

<https://doi.org/10.1038/s41524-024-01369-5>

Intrinsic single-layer multiferroics in transition-metal-decorated chromium trihalides

Check for updates

Meng Liu¹, Shuyi He¹, Hongyan Ji¹, Jingda Guo¹, Zhaotan Jiang², Jia-Tao Sun¹ & Hong-Jun Gao³

Two-dimensional materials possessing intrinsic multiferroic properties have long been sought to harness the magnetoelectric coupling in nanoelectronic devices. Here, we report the achievement of robust type I multiferroic order in single-layer chromium trihalides by decorating transition metal atoms. The out-of-plane ferroelectric polarization exhibits strong atomic selectivity, where 12 of 84 single-layer transition metal-based multiferroic materials possess out-of-plane ferroelectric or antiferroelectric polarization. Group theory reveals that this phenomenon is strongly dependent on $p-d$ coupling and crystal field splitting. Cu decoration enhances the intrinsic ferromagnetism of trihalides and increases the ferromagnetic transition temperature. Moreover, both ferroelectric and antiferroelectric phases are obtained, providing opportunities for electrical control of magnetism and energy storage and conversion applications. Furthermore, the transport properties of $\text{Cu}(\text{CrBr}_3)_2$ devices are calculated based on the non-equilibrium Green's function, and the results demonstrate outstanding spin-filtering properties and a low-bias negative differential resistance (NDR) effect for low power consumption.

Two-dimensional (2D) materials with multiferroic properties and possessing both ferromagnetism (FM) and ferroelectricity (FE) have attracted increasing amounts of attention among researchers for their fascinating physical properties and promising multifarious applications. FM and FE are crucial because of technological applications such as magnetic memory and ferroelectric memory^{1–3}. In conventional magnetoelectric multiferroics, magnetism usually originates from the partially filled d/f orbital of transition metal atoms, while electric polarization is usually caused by the off-center displacements of empty d/f orbital atoms⁴. The mutually exclusive requirements for the fully electronic occupation of the outer valence shell make it particularly challenging to achieve FM and FE simultaneously in the bulk material^{5–17}.

2D multiferroic semiconductors with atomic thickness have received considerable attention due to their ability to overcome these mutually exclusive requirement¹⁸. The out-of-plane FE in 2D magnetic materials is generally considered to decrease the depolarization field^{21,20}. Furthermore, polarization reversal in 2D ferroelectric materials with out-of-plane electric polarization can be achieved by an electric field in the vertical direction. To date, many 2D ferromagnetic materials, such as CrI_3 , VI_3 , VSe_2 , $\text{Cr}_2\text{Ge}_2\text{Te}_6$, and Fe_3GeTe_2 , etc., have been studied on the basis of theoretical or experimental results^{21–33}. Likewise, considerable progress has been achieved in ferroelectric materials^{34–53}. 2D ferroelectric materials such as SnTe , SnSe ,

and SnS thin films (several unit cells) have been shown to possess in-plane FE with critical transition temperature higher than those of their bulk phase^{45–48}. Other structural analogs of 2D SnTe MX ($M = \text{Ge}, \text{Sn}$; $X = \text{S}, \text{Se}$) or elemental ferroelectric bismuth were also predicted to exhibit in-plane FE^{51–55}. Only a few 2D ferroelectric materials with intrinsic out-of-plane polarization have been confirmed theoretically and experimentally, including $1T\text{-MoTe}_2$, CuInP_2S_6 (CIPS), and $\alpha\text{-In}_2\text{Se}_3$ ^{35,36,56–60}. In view of the large family of 2D magnetic materials, 2D multiferroic materials with out-of-plane electric polarization by made of 2D magnetic semiconductors are desirable for integrated nanodevices.

Monolayer CrX_3 ($X = \text{Cl}, \text{Br}, \text{I}$) is a prototypical Ising-type ferromagnet with out-of-plane magnetization^{21,61}. Many studies on the regulation of CrX_3 FM through strain, electron doping, and atom substitution doping have been conducted in recent years^{62–64}. Currently, most CrX_3 -based multiferroic devices are heterostructures composed of CrX_3 and an out-of-plane ferroelectric monolayer with a large thickness and nondegenerate polarized states^{65–69}. To our knowledge, little attention has been given to the effect of interstitial decoration on the ferroelectric and ferromagnetic properties of 2D CrX_3 ^{70–72}.

Herein, the large family of 2D $M(\text{CrX}_3)_2$ ($M =$ transition metal elements, $X = \text{Cl}/\text{Br}/\text{I}$) materials was systematically studied by first-principles

¹School of Integrated Circuits and Electronics, MIIT Key Laboratory for Low-Dimensional Quantum Structure and Devices, Beijing Institute of Technology, Beijing, China. ²School of Physics, Beijing Institute of Technology, Beijing, China. ³Beijing National Center for Condensed Matter Physics and Institute of Physics, Chinese Academy of Sciences, Beijing, China. e-mail: jtsun@bit.edu.cn

calculation. We identified 12 stable FM + FE out-of-plane single-layer multiferroic materials by decorating chromium trihalides using 28 transition metal elements. As a concrete example, we reveal that the Cu-decorated monolayer CrX_3 exhibits out-of-plane multiferroicity as a result of symmetry-controlled p - d coupling due to the crystal field effects. The decorated Cu atom fills one side of the hollow region, resulting in large permanent electric dipoles whose direction can be switched because of the lower transition barriers. In addition, the incorporation of Cu enhances the intrinsic FM of monolayer CrX_3 . Therefore, Cu-decorated monolayer CrX_3 is an ideal atomically thick 2D material, that possesses both permanent out-of-plane FE and FM, and has broad application prospects in nonvolatile memory nanodevices like electrets.

Results

Emergence of out-of-plane ferroelectricity in Cu-decorated chromium trihalides

Pristine CrX_3 monolayers belong to the $P\bar{3}1m$ space group which is centrosymmetric with no spontaneous electric polarization. The Cr atoms are arranged in a honeycomb lattice and are hexa coordinated by X atoms. We decorated a Cu atom at the center of the Cr honeycomb lattice. Figure 1a shows the atomic structure of monolayer $\text{Cu}(\text{CrX}_3)_2$ ($X = \text{Cl}/\text{Br}/\text{I}$). The dynamic stability of the $\text{Cu}(\text{CrX}_3)_2$ monolayer was subsequently confirmed by its phonon spectrum (without imaginary phonon modes) (Fig. S3). $\text{Cu}(\text{CrX}_3)_2$ is in the $P31m$ space group, and its spatial inversion symmetry is broken compared to that of CrX_3 . Due to the breaking of the inversion

symmetry induced by Cu decoration, the spatial separation of positive and negative charge centers in the out-of-plane direction (Fig. 2b) results in an unequal electrostatic potential at the top and bottom surfaces, respectively, producing an out-of-plane electric polarization vector.

As illustrated in Fig. 1b and Fig. S5, we label two typical sites of the Cu atom in the lattice according to its out-of-plane displacement: (i) the bond center site surrounded by six nonmetal atoms, labeled PE, and (ii) the in-plane (out-of-plane) tetrahedral site with three nonmetal atoms in close proximity, labeled FE and FE' (FE1 and FE1'). To elucidate the origin of the polarization of $\text{Cu}(\text{CrX}_3)_2$, two factors must be considered. First, the two sites have different local point symmetries. Second, the energy of the Cu d orbitals is similar to that of the X p orbitals (as shown in Fig. 1c). We name these p orbitals as the host p orbitals. Taking $\text{Cu}(\text{CrBr}_3)_2$ as an example, we classify all these sites into two types of symmetries:

(i) When the Cu atom occupies the bond center site (PE), the system has a O_h symmetry, which includes the irreducible representations $A_{1g}, A_{2g}, E_g, T_{1g}, T_{2g}, A_{1u}, A_{2u}, E_u, T_{1u}$ and T_{2u} . At the center of the Brillouin zone Γ , the Cu d orbitals are described by the E_g and T_{2g} representations, while the host unoccupied p state is described by the A_{1g} representation. Since there are no common representations between the Cu d orbitals and the host p orbital, the p - d coupling defined as $V_{p-d} = |\langle p|\Delta V|d_0\rangle|^2 / (\epsilon_p - \epsilon_d)$ is symmetrically forbidden, i.e., $V_{p-d} = 0^{73}$. (ii) When the Cu atom is an out-of-plane (in-plane) tetrahedral site (FE or FE' or FE1 or FE1'), the system reduces to C_{3v} due to the crystal field effect, in which the Cu d orbitals are described by the A_{1g} and E_g representations, and the host p state is described

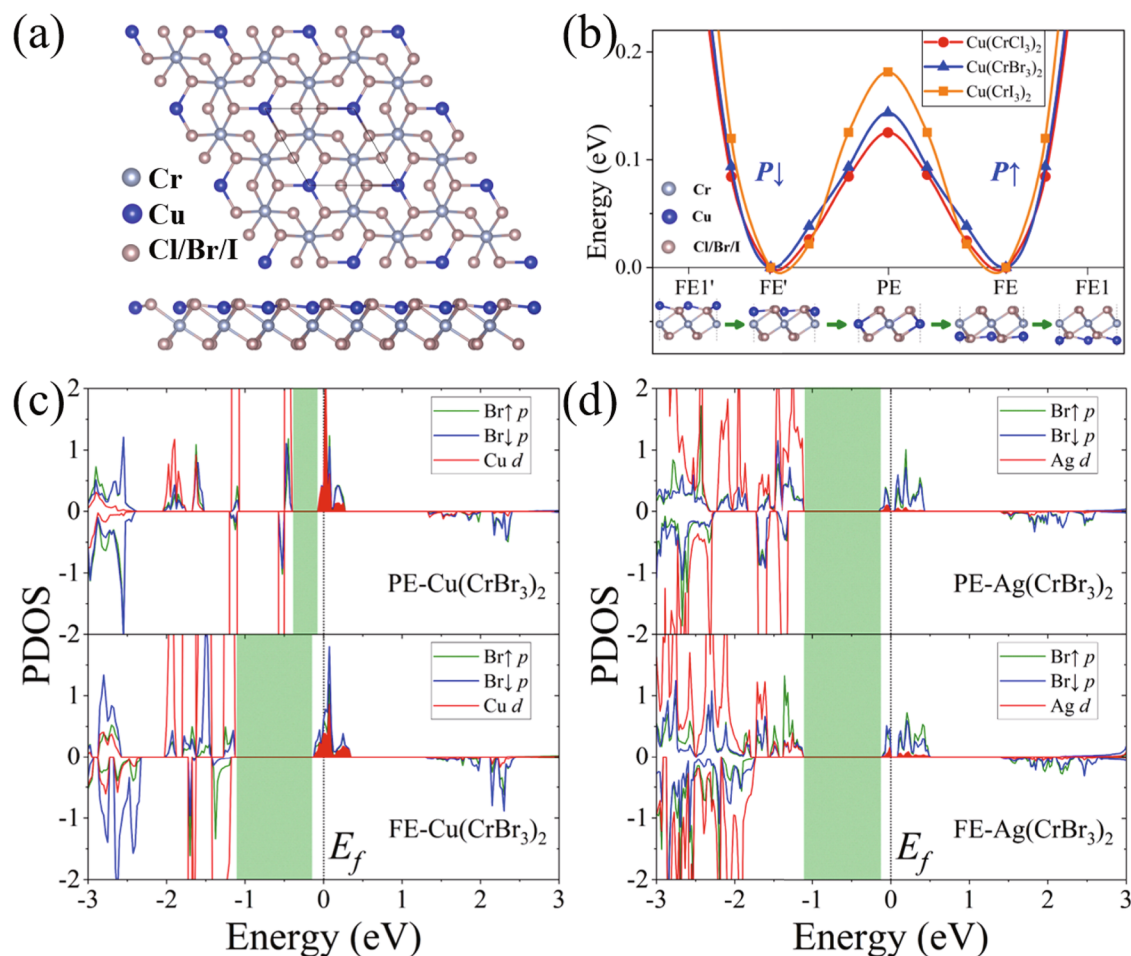


Fig. 1 | The structure and ferroelectric properties of $\text{Cu}(\text{CrX}_3)_2$. **a** Top and side views of monolayer $\text{Cu}(\text{CrX}_3)_2$ atomic structure. **b** The ferroelectric switching pathways of Cu in CrX_3 monolayers. The projected density of states (PDOS) for **c** $\text{Cu}(\text{CrBr}_3)_2$, and **d** $\text{Ag}(\text{CrBr}_3)_2$ monolayer calculated by DFT + U method. The

upper and lower panels represent the PE and FE phases, respectively. The Br \uparrow and Br \downarrow represent the upper and lower surfaces of Br atoms, respectively. The Br \downarrow atoms in the FE phase are slightly below Cu atoms. The contributions of Cu d and Ag d orbitals at the Fermi level (E_f) are highlighted.

Fig. 2 | The ferroelectric transition pathway, polarization origin and band structure of Cu(CrBr₃)₂. **a** Kinetics pathways of polarization reversal processes for Cu(CrBr₃)₂ structure. One FE state is taken as the initial state (left inset). **b** The reduced electron density difference along the *z* direction $\rho(z)$ for FE and PE states. The band structures of CrBr₃ (**c**) and Cu(CrBr₃)₂ (**d**). The inset in (**d**) is the spin-orbit coupling band structure of Cu(CrBr₃)₂.

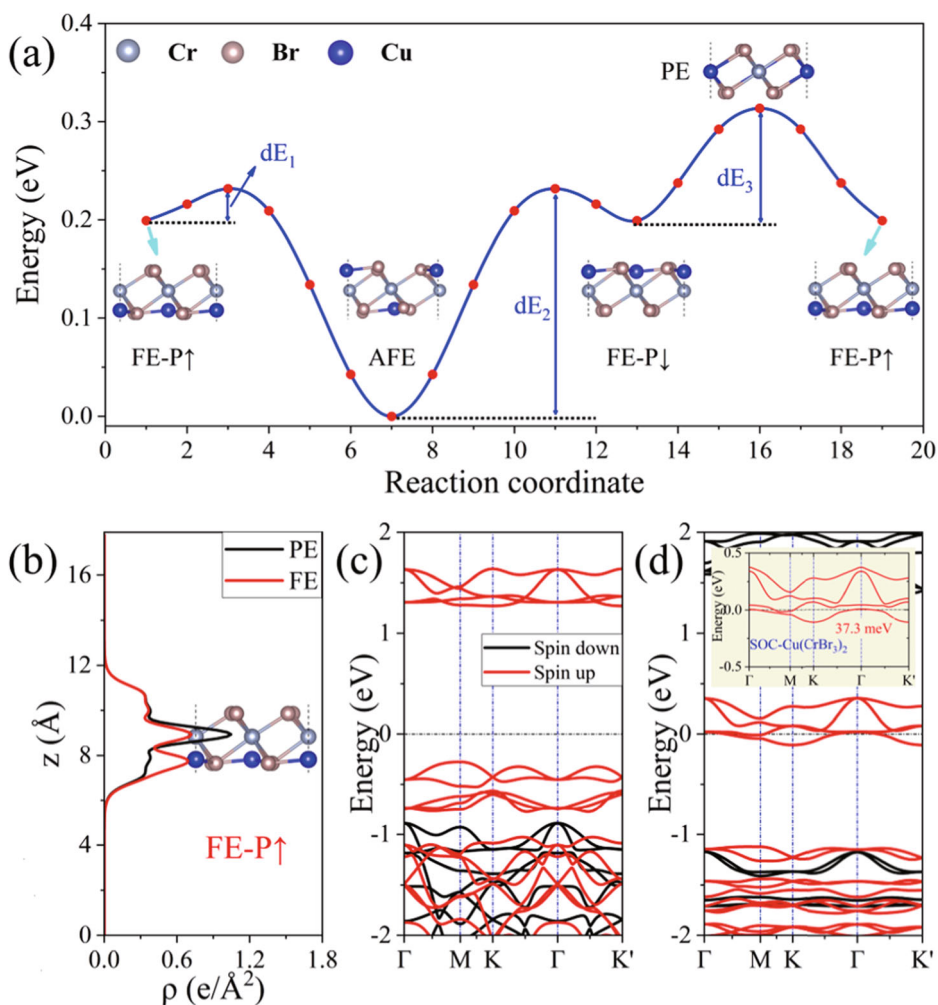


Table 1 | Irreducible representations of Cu *d* and host *p* orbitals in the *O_h* and *C_{3v}* point groups, respectively

Atom structure (point group)	Cu <i>d</i>	Host <i>p</i>	<i>p</i> - <i>d</i> coupling?
PE (<i>O_h</i>)	$E_g \oplus T_{2g} (\Gamma_5 \oplus \Gamma_3)$	$A_{1g} (\Gamma_1)$	No
FE (<i>C_{3v}</i>)	$A_{1g} \oplus E_g (\Gamma_3 \oplus \Gamma_1)$	$A_{1g} (\Gamma_1)$	Yes

Koster notations are shown in the parentheses for the reference. In the *O_h* symmetry, there is no *p*-*d* coupling between the Cu *d* and host *p* orbitals. In the *C_{3v}* symmetry, the *p*-*d* coupling is allowed.

by the *A_{1g}* representation. Consequently, the Cu *d* and host *p* orbitals could couple with each other ($V_{p-d} \neq 0$) because they are now described by a common representation (*A_{1g}*) (see Fig. S7).

A summary of the symmetry analysis is given in Table 1. When the Cu atom remains at the PE site there is no *p*-*d* coupling; when the Cu atom is at the in-plane (out-of-plane) tetrahedral site, *p*-*d* coupling is allowed. In addition, the strength of the *p*-*d* coupling increases as the ionicity of Cu(CrX₃)₂ increases since V_{p-d} is proportional to the difference between the anion and cation potentials. Note that, although *s*-*d* coupling may also be allowed in these systems, it does not have much effect on the ferroelectric transitioning since both the *s* and *d* orbitals are fully occupied.

To confirm the emergence of FE, we compute the potential energy along the ferroelectric transition path of Cu-decorated monolayer CrX₃ compounds. As shown in Fig. 1b, the ferroelectric transition paths are exactly along the (001) direction of the 2D material, i.e., from the FE' to the PE to the FE site as shown in Fig. 1b. Deviation of the Cu atom from the PE sites leads to *p*-*d* coupling decreasing the total energy, which is confirmed by the calculated electronic structure of Cu(CrBr₃)₂ as followed. Figure 1c

shows the projected density of states (PDOS) of the Br *p* orbital and Cu *d* orbital in the paraelectric and ferroelectric phases, respectively. The Br↑ and Br↓ represent the upper and lower surface Br atoms, respectively. The results show that the Cu *d* orbital and the neighboring Br *p* orbital strongly interact, resulting in *p*-*d* coupling around the Fermi level. Strong *p*-*d* coupling reduces the energy of the Br *p* and Cu *d* orbitals at the neighboring Fermi level (the first peak to the left of the light green area in Fig. 1c), thereby reducing the energy of the system. For the FE phase, the Br↓ atoms are close to the Cu plane. Therefore, the *p*-*d* coupling between the lower Br atoms and Cu atoms is stronger in the ferroelectric phase.

From the Cu(CrI₃)₂ to Cu(CrCl₃)₂ monolayer compounds, the *p*-*d* coupling strength and magnitude of charge transfer from the cation to the anion further increase due to the increased ionicity. For Cu atoms with high-lying *d* orbitals, the enhanced *p*-*d* coupling significantly increases the energy at the PE site, leading to an increase in the ferroelectric transition energy barrier (see Fig. 1b). Thus, in Cu-decorated chromium trihalides, the ferroelectric polarization originates from strong *p*-*d* coupling at the Fermi level.

Atomic selectivity of out-of-plane ferroelectricity

In addition to Cu atoms, Ag and Au atoms belong to the same family and have the same number of valence electrons as Cu. So, Ag and Au atoms were also used to decorate CrBr₃. Figure S5b shows the ferroelectric switching energy curves of single-layer CrBr₃ decorated with Cu, Ag, and Au atoms. The double-well potential energy curve shows that Cu and Au atom decoration can form two switchable ferroelectric phases. However, Ag decoration results in the formation of a paraelectric phase with a single potential well. Why does Ag atom decoration not result in a ferroelectric phase? To reveal the mechanism of the paraelectric state by Ag decoration, the calculated PDOS of Ag(CrBr₃)₂ is shown in Fig. 1d and Fig. S6. It is shown that Ag has lower 4d orbital levels (the 4d orbital energy of Ag is lower than that of the Cu 3d orbital⁷⁴). Consequently, the *p*–*d* coupling at the Fermi level is very weak. Figure S5a shows the atomic structure of the FE phase and PE phase of metal atoms decorated with monolayer CrBr₃. In the FE phase, the decorated atoms form a tetrahedral structure with three Br atoms. In the PE phase, the decorated atoms form an octahedral structure with six Br atoms. In the Ag(CrBr₃)₂ system, the *p*–*d* coupling is weak, and the Coulomb interaction competitive relationship between tetrahedral and octahedral fields plays a dominant role. From the PDOS (Fig. 1c, d and Fig. S6), we can see that the energy splitting (the gapped region shaded by the light green) of the tetrahedral crystal field of Cu and Au is much greater than that of the octahedral crystal field. In the Ag(CrBr₃)₂ system, the energy splitting of the tetrahedral crystal field is almost the same as that of the octahedral crystal field. This is beneficial for the formation of a PE phase with higher symmetry.

The above results indicate that in the M(CrBr₃)₂ (*M* = Cu/Ag/Au) system, if the *p*–*d* coupling is strong, an FE phase will form. If the *p*–*d* coupling is weak, a PE phase will be formed due to the effect of the octahedral crystal field Coulomb interaction. The emergence and stability of out-of-plane FE with strong atomic selectivity are intrinsic in transition-metal-decorated 2D magnetic semiconductors CrX₃, which has a great advantage over prior strontium oxide with soft phonon instability. The strong atomic selectivity discussed above is not limited to Cu and Au. After screening 28 transition metal atoms in the periodic table of elements, we identify 12 intrinsic single-layer multiferroic materials M(CrX₃)₂ possessing out-of-plane FE (see Fig. S1 and Table S1).

Single-layer out-of-plane ferroelectricity induced by decoration atoms

The intrinsic out-of-plane FE of nanometer-scale films is required to miniaturize electronic devices. We obtained the single-layer intrinsic out-of-plane ferroelectric material Cu(CrX₃)₂ by decorating Cu in monolayer CrX₃. Compared with that of CrX₃ (CrCl₃ = 6.061 Å, CrBr₃ = 6.448 Å, and CrI₃ = 7.081 Å), the lattice constant of Cu(CrX₃)₂ increased (see Table S3, Cu(CrCl₃)₂, Cu(CrBr₃)₂, and Cu(CrI₃)₂ increased by 4.37%, 3.44%, and 1.20%, respectively). The translation pathway, i.e., the ferroelectric transition pathway (dE₃), was computed by the climbing image nudged elastic band (CI-NEB) method⁷⁵, as shown in Fig. 2a and Fig. S9. The barrier of the Cu(CrCl₃)₂ system is about 125 meV/f.u., which is close to that of 2D ferroelectric In₂Se₃ (66 meV/f.u.) revealing the feasibility of ferroelectric switching under ambient conditions³⁶. The transition energy barrier of Cu(CrBr₃)₂ and Cu(CrI₃)₂ is slightly increased to 144 and 181 meV/f.u., respectively.

According to the charge center method, the calculated vertical polarization of Cu(CrCl₃)₂, Cu(CrBr₃)₂, and Cu(CrI₃)₂ are 14.98 × 10^{−12} C/m, 7.56 × 10^{−12} C/m, and 5.72 × 10^{−12} C/m, respectively (see Table S3), more than three times greater than that (2.08 × 10^{−12} C/m) of AB stacked BN reported previously, which is beneficial for the experimental measurements^{39,76}. Figure 2c, d shows the energy band structures of CrBr₃ and Cu(CrBr₃)₂, respectively. Cu(CrBr₃)₂ exhibits half-metallic properties compared with pristine magnetic semiconductor CrBr₃. This peculiar characteristic is highly desirable for spin-based devices (to be presented in Fig. 5)⁷⁷, such as magnetic tunneling junctions^{78,79}, spin field-effect transistors⁸⁰, and spin-light-emitting diodes⁸¹.

We also considered the antiferroelectric (AFE) phase of Cu(CrBr₃)₂, in which opposite electric dipole moments aligned in one lattice direction, as shown in Fig. S12. The AFE1 configuration is lower in energy than the FE and AFE2 phases, which is similar to the cases of FE Sc₂CO₂ and CuMP₂X₆ (*M* = Cr, V; *X* = S, Se)^{15,38}. The AFE1 phase belongs to the *P21/m* space group with inversion symmetry, so the overall electric polarization is zero. The energy barrier (dE₂ in Fig. 2a) for the transition from AFE1 to FE is lower than that of the previously reported Cu(CrI₃)₂, which demonstrates the AFE1 phases can be converted into FE phases using an external electric field⁷².

Enhanced magnetism and magnetic phase transition

Based on the above discussion, we have obtained single-layer intrinsic out-of-plane ferroelectric materials Cu(CrX₃)₂. Considering the intrinsic magnetism of CrX₃, it is necessary to evaluate the magnetic properties of Cu(CrX₃)₂. To assess the magnetic ground state, we analyzed the total energies of the different magnetic configurations (see Fig. S13), and the results are summarized in Table S4. The FM configuration is energetically favorable for all the Cu(CrX₃)₂ considered in our work, which indicates that the 2D FE Cu(CrX₃)₂ inherits the ferromagnetic ground state of CrX₃. The magnetic anisotropic energy (MAE) is evaluated as MAE = *E*_{in} − *E*_{out}, where *E*_{in} and *E*_{out} are the energies of CrX₃ systems with in-plane and out-of-plane magnetism, respectively. Positive and negative MAE values indicate out-of-plane and in-plane magnetic anisotropy, respectively. As shown in Table S4, the MAEs of CrCl₃, CrBr₃, and CrI₃ are 0.03, 0.21, and 0.77 meV/Cr atom, respectively, reflecting the out-of-plane magnetization of CrX₃, which is in agreement with previous results⁶³. However, the MAE of Cu(CrCl₃)₂ and Cu(CrI₃)₂ per Cr atom becomes negative, indicating that the spin magnetization axis is switched to the in-plane direction, which is distinct with that of Cu(CrBr₃)₂.

The Curie temperature (*T*_C) is estimated via Monte Carlo (MC) simulations based on the 2D Heisenberg model. The spin Hamiltonian is given by

$$H = -J \sum_{\langle i,j \rangle} S_i \cdot S_j - \sum_i A(S_i^2), \quad (1)$$

where *J* is the nearest-neighbor exchange parameter, *A* is the MAE parameter, and *S*_{*i*} and *S*_{*j*} are the spin operators which are assumed to be half of the calculated magnetic moment in this work. A supercell of 70 × 70 × 1 is adopted and 2 × 10⁷ steps are performed in the MC simulations. As shown in Fig. 3a, c and Table S4, the obtained Curie temperature *T*_C of pristine CrCl₃, CrBr₃, and CrI₃ are 21, 34, and 43 K, respectively, which are in agreement with experimental *T*_C data^{21–23}. Then, we calculate the *T*_C of single-layer Cu(CrX₃)₂. Compared with those of CrX₃, the obtained *T*_C of Cu(CrX₃)₂ is significantly enhanced due to the increased intralayer FM coupling.

Due to the octahedral crystal field, the Cr *d* orbitals in pristine CrX₃ systems split into threefold *t*_{2g} and twofold *e*_g manifolds. The lower *t*_{2g} orbitals are partially occupied, while the higher *e*_g orbitals are empty, making these systems magnetically semiconducting (Fig. 3d). Furthermore, in these monolayer CrX₃ systems, the Cr–X–Cr bond angle is close to 90°, and the FM semiconducting ground state is established via super-exchange interactions within the Cr–X–Cr configuration according to the well-known Goodenough–Kanamori–Anderson rules (Fig. 3b, d)^{82–84}. However, due to the competitive AFM interaction (i.e., Cr–Cr direct exchange), the overall FM coupling driven by super-exchange is quite weak. An in-depth study of the electronic structure of the CrX₃ monolayer may reveal similarities between them, that is the large energy gap between the occupied *t*_{2g}↑ and the empty *e*_g↑ orbitals (Fig. S7a–c). Huang et al. used a double-orbital model to prove that a larger virtual exchange gap (*E*_{ex}) is the key factor for weak FM coupling (Fig. 3d)⁸⁵. When the Cu decoration is introduced, the *e*_g↑ orbitals become partially occupied, enabling a decreased crystal field splitting energy (*E*_c); hence, *E*_{ex} decreases, and the FM coupling of Cu(CrX₃)₂ increases (see Fig. 3d and Table S2).

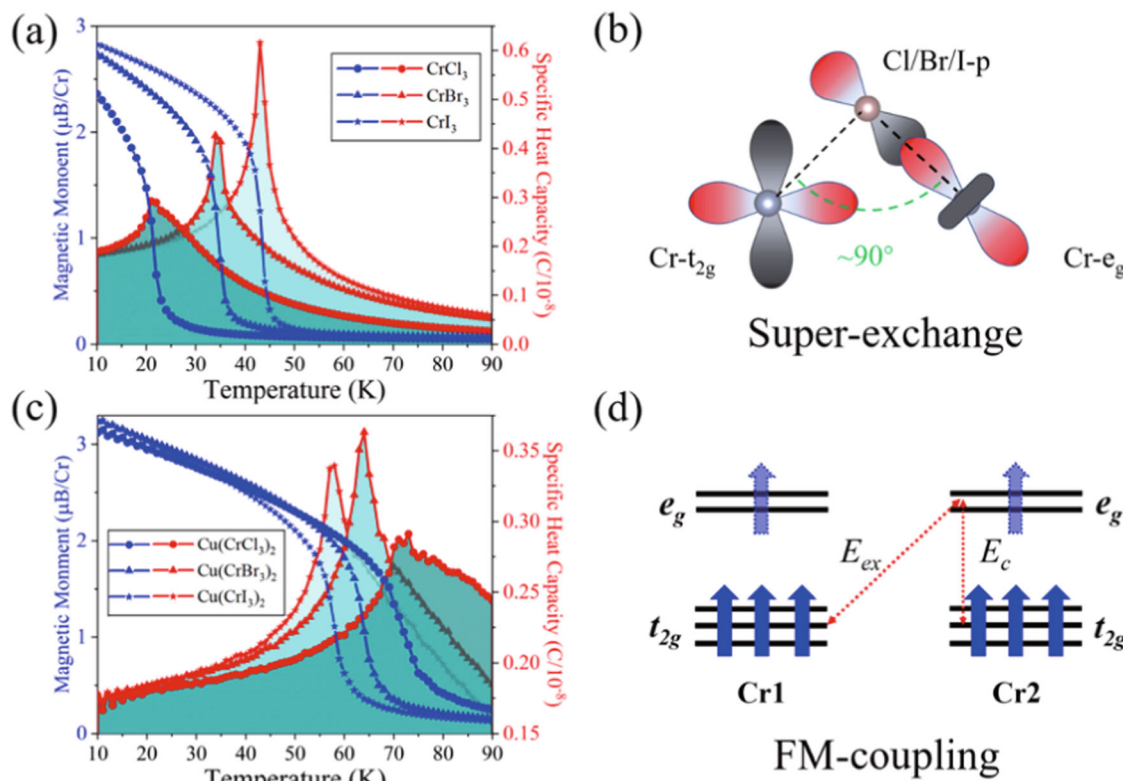


Fig. 3 | The magnetic properties of CrX₃ and Cu(CrX₃)₂. **a, c** The magnetic moment and specific heat capacity for monolayer CrX₃ and Cu(CrX₃)₂. **b** Schematic diagrams of the super-exchange interaction and FM coupling **(d)** in Cu(CrX₃)₂ monolayer.

Magnetolectric coupling

Given the prediction of the coexistence of FE and FM in Cu(CrX₃)₂, it is necessary to discuss the magnetolectric coupling effect of Cu(CrX₃)₂. To study the polarization switching of Cu(CrX₃)₂ under an external electric field, we investigate how applying a vertical electric field can reduce the transition barrier by breaking the degeneracy of the two polarization states. Notably, the energy barrier decreases significantly with increasing electric field (Fig. 4a and Fig. S14). We find that as the positive electric field increases, the energy of the P↓ state increases, while the energy of the P↑ state decreases, resulting in a sharp decrease in the energy barrier from P↓ to P↑. The results show that an electric field of 1.0 V/Å can produce an energy difference of 1.0 eV/f.u. in the Cu(CrCl₃)₂ system, which suggests that the critical electric field for reversing polarization is ~1.0 V/Å.

The intrinsic FE coercivity field can be estimated by determining the external electric field required to exceed the depolarization field. Landau–Devonshire phenomenology is used to determine the intrinsic coercive force field for continuous FE–PE first-order phase transitions. Taking the polarization *P* as the order parameter, the free energy *F* can be written as a power series expansion with respect to the polarization *P*⁸⁶:

$$F = \sum_i \left[\frac{\alpha}{2} P_i^2 + \frac{\beta}{4} P_i^4 + \frac{\gamma}{6} P_i^6 \right] - E \cdot P_i, \quad (2)$$

where *P_i* is the polarization of the *i*th unit cell, α , β , and γ are expansion coefficients, in which α takes the Curie–Weiss form $\alpha = \alpha_0(T - T_0)$, and *T*₀ is the Curie temperature⁸⁷. The electric field *E* is calculated from the minimum free energy density, which may be described by the Landau–Devonshire theory expanded in the electric polarization *P*: $E = \alpha P + \beta P^3 + \gamma P^5$, where the derivative relation gives the critical electric field exceeding the intrinsic coercive field *E_V* at the turning points of the function *P*(*E*). The magnitude of the intrinsic coercive field *E_V* is easily calculated from the extrema of Eq. (2).

The coercive field values of Cu(CrCl₃)₂, Cu(CrBr₃)₂, and Cu(CrI₃)₂, are calculated to be 1.0, 1.4, and 2.2 V/Å, respectively as shown in Fig. 4b. Notably, the magnitude of the critical electric field is similar to that of 2D In₂Se₃ (0.66 V/Å)³⁶, suggesting that the electric polarization of Cu(CrX₃)₂ can also be reversed by an appropriate vertically applied electric field⁵⁹. Interestingly, in the Cu(CrBr₃)₂ system, different electric ordering coupling occurs with different magnetic ordering, and the magnetism is determined by electric ordering which can be controlled by a gate field (Fig. 4c). Specifically, there are two phases in the Cu(CrBr₃)₂ system, namely, AFE–FM_{in} (in-plane FM) phase and the FE–FM_{out} (out-of-plane FM) phase as shown in Fig. 4c and Fig. S15. Unlike traditional multiferroics, where the magnetolectric coupling allows one to adjust the amplitude, here the coupling behaves like a logic operation, allowing one to radically change the ordering and phase transitions.

Spin-polarized transport of Cu(CrBr₃)₂ devices

In view of the semiconducting and half-metallic nature of CrX₃ and their ferroelectric characteristics, a two-probe device with distinct ferroelectric polarity in each electrode is constructed to study the spin-polarized transport. The PE–FE and FE–AFE configurations are denoted in subpanels A and B of Fig. 5a, respectively. As shown in Fig. 5b, the spin-down current of PE–FE or FE–AFE configuration is completely forbidden throughout the bias range for any device or transport direction, indicating that both devices can filter tunneling electrons based on their spin state and potentially serve as spin filters. Additionally, within the bias range from –0.1 to 0.1 V, the PE–FE device exhibits a larger non-equilibrium electric current at a certain bias than the FE–AFE Cu(CrBr₃)₂ device, which corresponds to the larger differential conductance (dI/dV) in the PE–FE device as shown in Fig. 5c. On the other hand, both devices can exhibit negative differential resistance (NDR) in a larger range of positive or negative bias, which is the basis for many device applications including high-frequency oscillators, analog-to-digital converters, and logic gates^{88–90}. The PE–FE Cu(CrBr₃)₂ device exhibits

Fig. 4 | Magnetoelectric coupling properties of $\text{Cu}(\text{CrX}_3)_2$. **a** Energy versus polarization under a vertical external electric field in $\text{Cu}(\text{CrCl}_3)_2$. **b** Theoretical ferroelectric hysteresis loops obtained from the first-order Landau–Ginzburg model for $\text{Cu}(\text{CrCl}_3)_2$, $\text{Cu}(\text{CrBr}_3)_2$, and $\text{Cu}(\text{CrI}_3)_2$. **c** The P – E hysteretic loop with the corresponding electric and magnetic ordering.

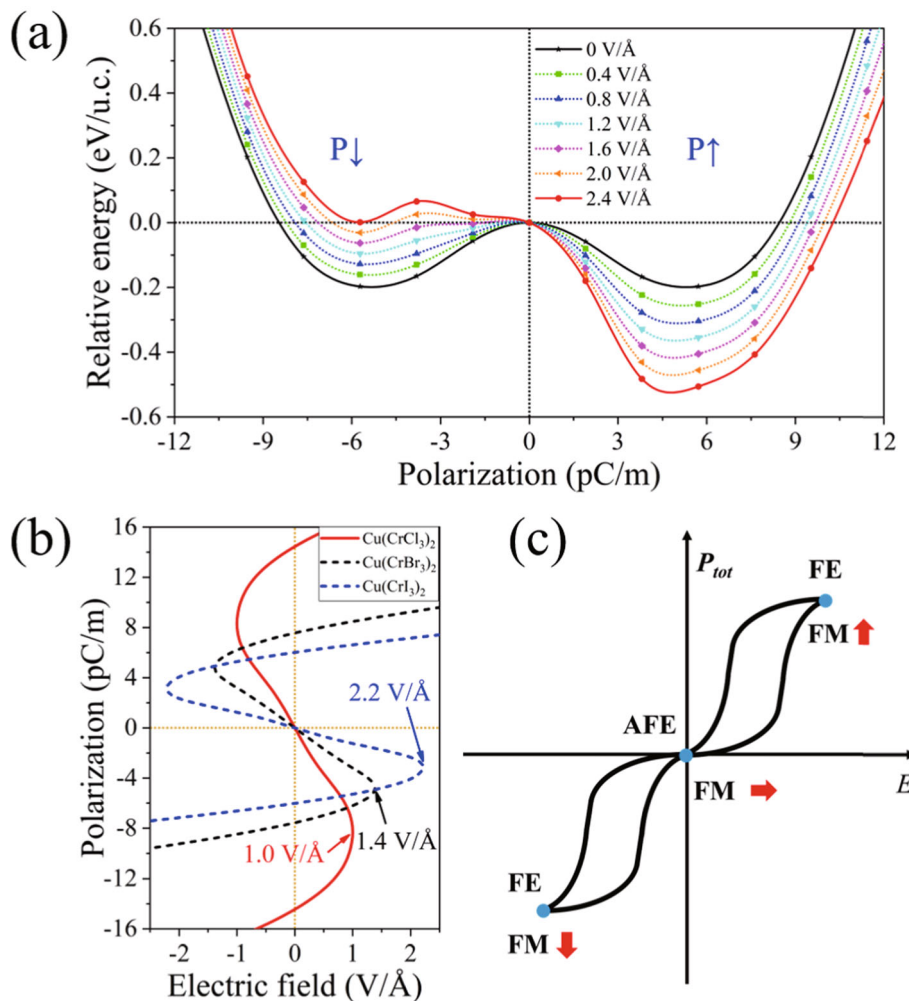
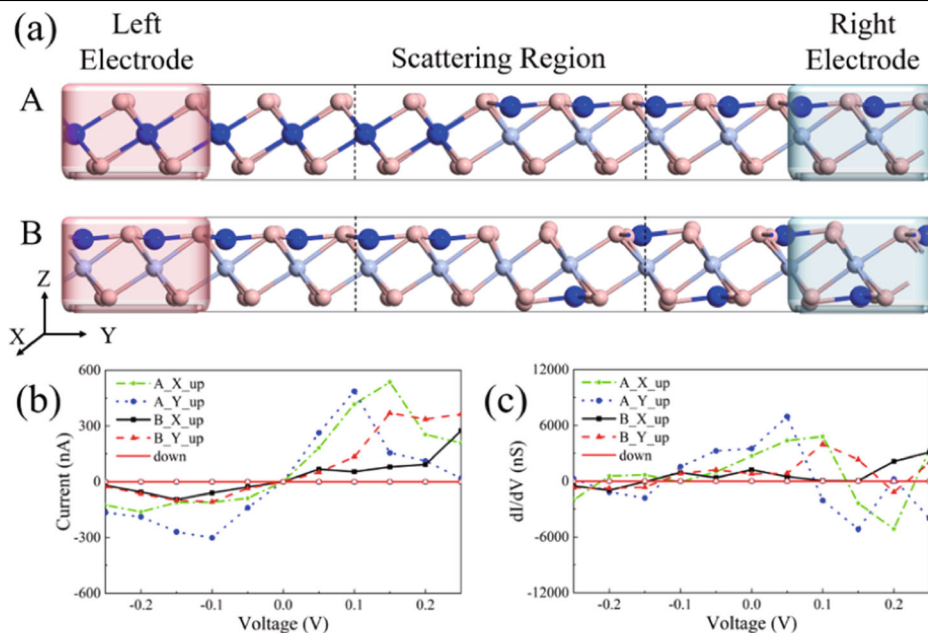


Fig. 5 | Spin-polarized transport of $\text{Cu}(\text{CrBr}_3)_2$ devices. **a** Schematic diagram of the devices of the PE-FE and FE-AFE $\text{Cu}(\text{CrBr}_3)_2$ with spin-resolved current–voltage (I – V) curves (**b**) and differential conductance (dI/dV) curves (**c**) in X and Y directions. The solid lines correspond to the nonzero spin-up current and the hollow lines correspond to the zero spin-down current. A and B represent PE-FE and FE-AFE $\text{Cu}(\text{CrBr}_3)_2$ devices, respectively.



significant NDR effects in the X and Y directions when the bias voltage exceeds 0.15 and 0.1 V, respectively. This observation can be further validated by the ratio of dI/dV with respect to the applied voltage. As shown in Fig. 5c, the PE-FE Cu(CrBr₃)₂ device exhibits negative dI/dV values for both the X and Y directions at 0.15 and 0.1 V, respectively. A small NDR effect is observed in the Y direction of the FE-AFE Cu(CrBr₃)₂ device at 0.15 and -0.1 V, and this effect in both the X and Y directions is almost completely quenched to zero at a negative bias of -0.25 V. Although NDR behaviors have been realized in many nanoscale systems, they usually occur at relatively high biases. Then the Cu(CrBr₃)₂ devices with low-bias NDR are desirable from the point view of power consumption.

Discussion

In summary, based on the combination of first-principles calculations and group symmetry analysis, we discussed the important role of Coulomb interactions in octahedral crystal fields and crystal symmetry forced p - d coupling in determining the decorating behavior of Cu, Ag, and Au in chromium trihalide semiconductors. When CrX₃ is decorated with Cu or Au, the p - d coupling effect is stronger than the Coulomb interaction of the octahedral crystal field, so Cu(CrX₃)₂ and Au(CrX₃)₂ possess intrinsic ferroelectric phases due to their structural stability. However, when Ag is decorated with CrX₃, Ag(CrX₃)₂ takes a paraelectric phase since the p - d coupling is weaker than the octahedral Coulomb interaction. After screening 28 transition metal elements, we identify that 12 M(CrX₃)₂ possesses the out-of-plane FE exhibiting the strong atomic selectivity. Atomic decoration can not only result in large out-of-plane electric polarization with a low energy barrier and tunable reversal electric field, but also enhanced intralayer FM coupling, giving rise to a higher Curie temperature. There are two phases AFE-FM_{in} and FE-FM_{out} in the Cu(CrBr₃)₂ system, which inspires ideas for the design of logical magnetoelectric coupling devices. In addition, Cu(CrBr₃)₂ devices demonstrate outstanding spin-filtering transmission and exhibit a low-bias NDR effect for low power consumption. This study provides theoretical guidance for the application of 2D ferromagnetic materials such as 2D CrX₃ in the design of multiferroic devices.

Methods

First-principles calculations of atomistic and electronic structure

Spin-polarized density-functional theory (DFT) first-principles calculations were carried out with the Vienna ab initio simulation package (VASP)^{91,92}. The projector augmented wave method was employed to describe the interaction between the core and valence electrons⁹³. The Perdew, Burke, and Ernzerhof parameterized gradient approximation is chosen to describe the exchange-correction functional⁹⁴. The CI-NEB method is used to calculate the energy barriers of transition states⁹⁵. In addition, for all the calculations, the cut-off energy for the basis set is chosen to be 500 eV. All geometric structures are fully relaxed until the force on each atom is <0.001 eV/Å, and the convergence criterion is 10⁻⁶ eV for energy. A vacuum space of 20 Å along the z direction was adopted to avoid spurious interactions between adjacent layers. The k -points sampling was performed with Monkhorst-Pack grids of 12 × 12 × 1. The on-site effective Hubbard interaction U was taken to be 0.5 eV in considering the electron correlation of 3d electrons of Cr atoms. Phonon dispersion relations are then acquired employing the PHONOPY code⁹⁵ with the finite displacement approach and the adapted 3 × 3 × 1 supercell is large enough to evaluate the dynamical stability. Then, we chose the Heisenberg model to simulate the Curie temperature of our systems based on the MC simulation. The software package developed by Zhang et al.⁹⁶, and the 70 × 70 × 1 lattice is used in the MC simulation.

Calculation of the electron transport properties in Cu(CrBr₃)₂

The calculation of the electron transport properties is implemented by Quantum Atomistix Toolkit (ATK) package⁹⁷, which is based on the DFT and the non-equilibrium Green's function. The spin-polarized generalized gradient approximation (SGGA) with the parametrization of Perdew–Burke–Ernzerhof (PBE), the cut-off energy of 310 Ry and a basis set of

double-zeta polarized are used. A vacuum slab of 15 Å is added between the nearest neighboring layers to eliminate their coupling. The Monkhorst-Pack k -mesh is chosen to be 1 × 5 × 150. Using the non-equilibrium Green's function formalism, the transmission coefficient $T(E)$ is calculated as⁹⁸

$$T(E) = T_r [\Gamma_L G_r \Gamma_R G^a], \quad (3)$$

where $G^{r(a)}$ is the retarded (advanced) Green's function, and $\Gamma_L(\Gamma_R)$ is the coupling of the central region to the left (right) lead. And the current is calculated by the Landauer–Büttiker formula, which is written as⁹⁹

$$I(V) = \frac{2e}{h} \int_{-\infty}^{\infty} T(E) [f(E - \mu_L) - f(E - \mu_R)] dE, \quad (4)$$

where $f(E - \mu_{L(R)})$ is the Fermi–Dirac distribution function of the left (right) electrode, where $\mu_{L(R)}$ is the electrochemical potential of the left (right) electrode.

Data availability

The data supporting the findings of this study are available within this article and its Supplementary Information. Additional data that support the findings of this study are available from the corresponding author on reasonable requests.

Code availability

The related codes are available from the corresponding author on reasonable requests.

Received: 2 February 2024; Accepted: 25 July 2024;

Published online: 14 August 2024

References

- Åkerman, J. Toward a universal memory. *Science* **308**, 508–510 (2005).
- Dawber, M., Rabe, K. M. & Scott, J. F. Physics of thin-film ferroelectric oxides. *Rev. Mod. Phys.* **77**, 1083–1130 (2005).
- Martin, L. W. & Rappe, A. M. Thin-film ferroelectric materials and their applications. *Nat. Rev. Mater.* **2**, 16087 (2016).
- Hill, N. A. Why are there so few magnetic ferroelectrics? *J. Phys. Chem. B* **104**, 6694–6709 (2000).
- Zhang, J. et al. Design of two-dimensional multiferroics with direct polarization-magnetization coupling. *Phys. Rev. Lett.* **125**, 017601 (2020).
- Xu, M. et al. Electrical control of magnetic phase transition in a type-I multiferroic double-metal trihalide monolayer. *Phys. Rev. Lett.* **124**, 067602 (2020).
- Ding, N., Chen, J., Dong, S. & Stroppa, A. Ferroelectricity and ferromagnetism in a VO₂ monolayer: role of the Dzyaloshinskii–Moriya interaction. *Phys. Rev. B* **102**, 165129 (2020).
- Zhang, T., Xu, X., Dai, Y., Huang, B. & Ma, Y. Intrinsic ferromagnetic triferroicity in bilayer T'-VTe₂. *Appl. Phys. Lett.* **120**, 192903 (2022).
- Liu, X., Pyatakov, A. P. & Ren, W. Magnetoelectric coupling in multiferroic bilayer VS₂. *Phys. Rev. Lett.* **125**, 247601 (2020).
- Zhao, Y. et al. Multiferroicity in a two-dimensional non-van der Waals crystal of AgCr₂X₄ (X = S or Se). *J. Phys. Chem. Lett.* **13**, 11346–11353 (2022).
- Tan, H. et al. Two-dimensional ferromagnetic-ferroelectric multiferroics in violation of the d⁰ rule. *Phys. Rev. B* **99**, 195434 (2019).
- Lai, Y. et al. Two-dimensional ferromagnetism and driven ferroelectricity in van der Waals CuCrP₂S₆. *Nanoscale* **11**, 5163–5170 (2019).
- Luo, W., Xu, K. & Xiang, H. Two-dimensional hyperferroelectric metals: a different route to ferromagnetic-ferroelectric multiferroics. *Phys. Rev. B* **96**, 235415 (2017).
- Sun, Y. et al. Two-dimensional multiferroic FeCl with room temperature ferromagnetism and tunable magnetic anisotropy via ferroelectricity. *J. Mater. Chem. C* **9**, 9197–9202 (2021).

15. Qi, J., Wang, H., Chen, X. & Qian, X. Two-dimensional multiferroic semiconductors with coexisting ferroelectricity and ferromagnetism. *Appl. Phys. Lett.* **113**, 043102 (2018).
16. Zhang, J.-J. et al. Type-II multiferroic Hf₂VC₂F₂ MXene monolayer with high transition temperature. *J. Am. Chem. Soc.* **140**, 9768–9773 (2018).
17. Chen, S. et al. Unconventional distortion induced two-dimensional multiferroicity in a CrO₃ monolayer. *Nanoscale* **13**, 13048–13056 (2021).
18. Novoselov, K. S. et al. Electric field effect in atomically thin carbon films. *Science* **306**, 666–669 (2004).
19. Batra, I. P., Wurfel, P. & Silverman, B. D. New type of first-order phase transition in ferroelectric thin films. *Phys. Rev. Lett.* **30**, 384–387 (1973).
20. Zhong, W., King-Smith, R. D. & Vanderbilt, D. Giant LO-TO splittings in perovskite ferroelectrics. *Phys. Rev. Lett.* **72**, 3618–3621 (1994).
21. Huang, B. et al. Layer-dependent ferromagnetism in a van der Waals crystal down to the monolayer limit. *Nature* **546**, 270–273 (2017).
22. Zhang, Z. et al. Direct photoluminescence probing of ferromagnetism in monolayer two-dimensional CrBr₃. *Nano Lett.* **19**, 3138–3142 (2019).
23. McGuire, M. A., Dixit, H., Cooper, V. R. & Sales, B. C. Coupling of crystal structure and magnetism in the layered, ferromagnetic insulator CrI₃. *Chem. Mater.* **27**, 612–620 (2015).
24. Gong, C. et al. Discovery of intrinsic ferromagnetism in two-dimensional van der Waals crystals. *Nature* **546**, 265–269 (2017).
25. Tian, S. et al. Ferromagnetic van der Waals crystal V₁I₃. *J. Am. Chem. Soc.* **141**, 5326–5333 (2019).
26. Cai, X. et al. Atomically thin CrCl₃: an in-plane layered antiferromagnetic insulator. *Nano Lett.* **19**, 3993–3998 (2019).
27. Bonilla, M. et al. Strong room-temperature ferromagnetism in VSe₂ monolayers on van der Waals substrates. *Nat. Nanotech.* **13**, 289–293 (2018).
28. Li, J. et al. Synthesis of ultrathin metallic MTe₂ (M = V, Nb, Ta) single-crystalline nanoplates. *Adv. Mater.* **30**, 1801043 (2018).
29. Fei, Z. et al. Two-dimensional itinerant ferromagnetism in atomically thin Fe₃GeTe₂. *Nat. Mater.* **17**, 778–782 (2018).
30. May, A. F. et al. Ferromagnetism near room temperature in the cleavable van der Waals crystal Fe₅GeTe₂. *ACS Nano* **13**, 4436–4442 (2019).
31. Deng, Y. et al. Quantum anomalous Hall effect in intrinsic magnetic topological insulator MnBi₂Te₄. *Science* **367**, 895–900 (2020).
32. Burch, K. S., Mandrus, D. & Park, J.-G. Magnetism in two-dimensional van der Waals materials. *Nature* **563**, 47–52 (2018).
33. van der Laan, G. Magnetic linear X-ray dichroism as a probe of the magnetocrystalline anisotropy. *Phys. Rev. Lett.* **82**, 640–643 (1999).
34. Wu, M., Burton, J. D., Tsymbal, E. Y., Zeng, X. C. & Jena, P. Hydroxyl-decorated graphene systems as candidates for organic metal-free ferroelectrics, multiferroics, and high-performance proton battery cathode materials. *Phys. Rev. B* **87**, 081406 (2013).
35. Shirodkar, S. N. & Waghmare, U. V. Emergence of ferroelectricity at a metal-semiconductor transition in a 1T monolayer of MoS₂. *Phys. Rev. Lett.* **112**, 157601 (2014).
36. Ding, W. et al. Prediction of intrinsic two-dimensional ferroelectrics in In₂Se₃ and other III₂-VI₃ van der Waals materials. *Nat. Commun.* **8**, 14956 (2017).
37. Wu, M., Dong, S., Yao, K., Liu, J. & Zeng, X. C. Ferroelectricity in covalently functionalized two-dimensional materials: integration of high-mobility semiconductors and nonvolatile memory. *Nano Lett.* **16**, 7309–7315 (2016).
38. Chandrasekaran, A., Mishra, A. & Singh, A. K. Ferroelectricity, antiferroelectricity, and ultrathin 2d electron/hole gas in multifunctional monolayer MXene. *Nano Lett.* **17**, 3290–3296 (2017).
39. Li, L. & Wu, M. Binary compound bilayer and multilayer with vertical polarizations: two-dimensional ferroelectrics, multiferroics, and nanogenerators. *ACS Nano* **11**, 6382–6388 (2017).
40. Bruyer, E. et al. Possibility of combining ferroelectricity and Rashba-like spin splitting in monolayers of the 1T-type transition-metal dichalcogenides MX₂ (M = Mo, W; X = S, Se, Te). *Phys. Rev. B* **94**, 195402 (2016).
41. Xiao, C. et al. Elemental ferroelectricity and antiferroelectricity in Group-V monolayer. *Adv. Funct. Mater.* **28**, 1707383 (2018).
42. Belianinov, A. et al. CuInP₂S₆ room temperature layered ferroelectric. *Nano Lett.* **15**, 3808–3814 (2015).
43. Li, W. et al. Emergence of ferroelectricity in a nonferroelectric monolayer. *Nat. Commun.* **14**, 2757 (2023).
44. Cheema, S. S. et al. Emergent ferroelectricity in subnanometer binary oxide films on silicon. *Science* **376**, 648–652 (2022).
45. Bao, Y. et al. Gate-tunable in-plane ferroelectricity in few-layer SnS. *Nano Lett.* **19**, 5109–5117 (2019).
46. Chang, K. et al. Discovery of robust in-plane ferroelectricity in atomic-thick SnTe. *Science* **353**, 274–278 (2016).
47. Chang, K. et al. Microscopic manipulation of ferroelectric domains in SnSe monolayers at room temperature. *Nano Lett.* **20**, 6590–6597 (2020).
48. Higashitarumizu, N. et al. Purely in-plane ferroelectricity in monolayer SnS at room temperature. *Nat. Commun.* **11**, 2428 (2020).
49. Wan, Y. et al. Room-temperature ferroelectricity in 1T'-ReS₂ multilayers. *Phys. Rev. Lett.* **128**, 067601 (2022).
50. Chyashnavichyus, M. et al. Size-effect in layered ferroelectric CuInP₂S₆. *Appl. Phys. Lett.* **109**, 172901 (2016).
51. Wu, M. & Zeng, X. C. Intrinsic ferroelasticity and/or multiferroicity in two-dimensional phosphorene and phosphorene analogues. *Nano Lett.* **16**, 3236–3241 (2016).
52. Fei, R., Kang, W. & Yang, L. Ferroelectricity and phase transitions in monolayer group-IV monochalcogenides. *Phys. Rev. Lett.* **117**, 097601 (2016).
53. Gou, J. et al. Two-dimensional ferroelectricity in a single-element bismuth monolayer. *Nature* **617**, 67–72 (2023).
54. Wang, H. & Qian, X. Two-dimensional multiferroics in monolayer group IV monochalcogenides. *2D Mater.* **4**, 015042 (2017).
55. Wan, W., Liu, C., Xiao, W. & Yao, Y. Promising ferroelectricity in 2D group IV tellurides: a first-principles study. *Appl. Phys. Lett.* **111**, 132904 (2017).
56. Yuan, S. et al. Room-temperature ferroelectricity in MoTe₂ down to the atomic monolayer limit. *Nat. Commun.* **10**, 1775 (2019).
57. Liu, F. et al. Room-temperature ferroelectricity in CuInP₂S₆ ultrathin flakes. *Nat. Commun.* **7**, 12357 (2016).
58. Zhou, Y. et al. Out-of-plane piezoelectricity and ferroelectricity in layered α-In₂Se₃ nanoflakes. *Nano Lett.* **17**, 5508–5513 (2017).
59. Cui, C. et al. Intercorrelated in-plane and out-of-plane ferroelectricity in ultrathin two-dimensional layered semiconductor In₂Se₃. *Nano Lett.* **18**, 1253–1258 (2018).
60. Zhang, X. et al. Origin of versatile polarization state in CuInP₂S₆. *Phys. Rev. B* **108**, L161406 (2023).
61. Kulish, V. V. & Huang, W. Single-layer metal halides MX₂ (X = Cl, Br, I): stability and tunable magnetism from first principles and Monte Carlo simulations. *J. Mater. Chem. C* **5**, 8734–8741 (2017).
62. Jiang, S., Li, L., Wang, Z., Mak, K. F. & Shan, J. Controlling magnetism in 2D CrI₃ by electrostatic doping. *Nat. Nanotech.* **13**, 549–553 (2018).
63. Webster, L. & Yan, J.-A. Strain-tunable magnetic anisotropy in monolayer CrCl₃, CrBr₃, and CrI₃. *Phys. Rev. B* **98**, 144411 (2018).
64. Wu, Z., Yu, J. & Yuan, S. Strain-tunable magnetic and electronic properties of monolayer CrI₃. *Phys. Chem. Chem. Phys.* **21**, 7750–7755 (2019).
65. Zhao, Y., Zhang, J.-J., Yuan, S. & Chen, Z. Nonvolatile electrical control and heterointerface-induced half-metallicity of 2D ferromagnets. *Adv. Funct. Mater.* **29**, 1901420 (2019).
66. Lu, Y. et al. Artificial multiferroics and enhanced magnetoelectric effect in van der Waals heterostructures. *ACS Appl. Mater. Interfaces* **12**, 6243–6249 (2020).

67. Cheng, H.-X., Zhou, J., Wang, C., Ji, W. & Zhang, Y.-N. Nonvolatile electric field control of magnetism in bilayer CrI₃ on monolayer In₂Se₃. *Phys. Rev. B* **104**, 064443 (2021).
68. Pei, Q., Zhou, B., Mi, W. & Cheng, Y. Triferroic material and electrical control of valley degree of freedom. *ACS Appl. Mater. Interfaces* **11**, 12675–12682 (2019).
69. Yang, B. et al. Realization of semiconducting layered multiferroic heterojunctions via asymmetrical magnetoelectric coupling. *Phys. Rev. B* **103**, L201405 (2021).
70. Huang, C. et al. Prediction of intrinsic ferromagnetic ferroelectricity in a transition-metal halide monolayer. *Phys. Rev. Lett.* **120**, 147601 (2018).
71. Zhao, Y. et al. Surface vacancy-induced switchable electric polarization and enhanced ferromagnetism in monolayer metal trihalides. *Nano Lett.* **18**, 2943–2949 (2018).
72. Zhang, L., Tang, C. & Du, A. Tri-coordinated Au dopant induced out-of-plane ferroelectricity and enhanced ferromagnetism in chromium triiodide. *J. Mater. Chem. C* **11**, 1111–1118 (2023).
73. Huang, B., Xiang, H., Yu, J. & Wei, S.-H. Effective control of the charge and magnetic states of transition-metal atoms on single-layer boron nitride. *Phys. Rev. Lett.* **108**, 206802 (2012).
74. Deng, H.-X., Luo, J.-W., Li, S.-S. & Wei, S.-H. Origin of the distinct diffusion behaviors of Cu and Ag in covalent and ionic semiconductors. *Phys. Rev. Lett.* **117**, 165901 (2016).
75. Henkelman, G., Uberuaga, B. P. & Jónsson, H. A climbing image nudged elastic band method for finding saddle points and minimum energy paths. *J. Chem. Phys.* **113**, 9901–9904 (2000).
76. Liu, M. et al. Orbital distortion and electric field control of sliding ferroelectricity in a boron nitride bilayer. *J. Phys. Condens. Matter* **35**, 235001 (2023).
77. Li, R., Jiang, J., Shi, X., Mi, W. & Bai, H. Two-dimensional janus FeXY (X, Y = Cl, Br, and I, X ≠ Y) monolayers: half-metallic ferromagnets with tunable magnetic properties under strain. *ACS Appl. Mater. Interfaces* **13**, 38897–38905 (2021).
78. Li, M.-R. et al. Giant magnetoresistance in the half-metallic double-perovskite ferrimagnet Mn₂FeReO₆. *Angew. Chem. Int. Ed.* **54**, 12069–12073 (2015).
79. Kobayashi, K. I., Kimura, T., Sawada, H., Terakura, K. & Tokura, Y. Room-temperature magnetoresistance in an oxide material with an ordered double-perovskite structure. *Nature* **395**, 677–680 (1998).
80. Sugahara, S. & Tanaka, M. A spin metal–oxide–semiconductor field-effect transistor using half-metallic-ferromagnet contacts for the source and drain. *Appl. Phys. Lett.* **84**, 2307–2309 (2004).
81. Wang, J. et al. Spin-optoelectronic devices based on hybrid organic-inorganic trihalide perovskites. *Nat. Commun.* **10**, 129 (2019).
82. Anderson, P. W. Antiferromagnetism. Theory of superexchange interaction. *Phys. Rev.* **79**, 350–356 (1950).
83. Goodenough, J. B. Theory of the role of covalence in the perovskite-type manganites [La, M(II)]MnO₃. *Phys. Rev.* **100**, 564–573 (1955).
84. Kanamori, J. Superexchange interaction and symmetry properties of electron orbitals. *J. Phys. Chem. Solids* **10**, 87–98 (1959).
85. Huang, C. et al. Toward intrinsic room-temperature ferromagnetism in two-dimensional semiconductors. *J. Am. Chem. Soc.* **140**, 11519–11525 (2018).
86. Vitalii, L. G. Phase transitions in ferroelectrics: some historical remarks. *Phys.-Uspekhi* **44**, 1037 (2001).
87. Liu, Y., Lou, X., Bibes, M. & Dkhil, B. Effect of a built-in electric field in asymmetric ferroelectric tunnel junctions. *Phys. Rev. B* **88**, 024106 (2013).
88. Brown, E. R. et al. Oscillations up to 712 GHz in InAs/AlSb resonant-tunneling diodes. *Appl. Phys. Lett.* **58**, 2291–2293 (1991).
89. Broekaert, T. P. E. et al. A monolithic 4-bit 2-Gsps resonant tunneling analog-to-digital converter. *IEEE J. Solid State Circuits* **33**, 1342–1349 (1998).
90. Mathews, R. H. et al. A new RTD-FET logic family. *Proc. IEEE* **87**, 596–605 (1999).
91. Kresse, G. & Hafner, J. Ab initio molecular dynamics for liquid metals. *Phys. Rev. B* **47**, 558–561 (1993).
92. Kresse, G. & Furthmüller, J. Efficient iterative schemes for ab initio total-energy calculations using a plane-wave basis set. *Phys. Rev. B* **54**, 11169–11186 (1996).
93. Blöchl, P. E. Projector augmented-wave method. *Phys. Rev. B* **50**, 17953–17979 (1994).
94. Perdew, J. P., Burke, K. & Ernzerhof, M. Perdew, Burke, and Ernzerhof reply. *Phys. Rev. Lett.* **80**, 891–891 (1998).
95. Togo, A. & Tanaka, I. First principles phonon calculations in materials science. *Scr. Mater.* **108**, 1–5 (2015).
96. Zhang, Y., Wang, B., Guo, Y., Li, Q. & Wang, J. A universal framework for metropolis Monte Carlo simulation of magnetic Curie temperature. *Comput. Mater. Sci.* **197**, 110638 (2021).
97. Smidstrup, S. et al. QuantumATK: an integrated platform of electronic and atomic-scale modelling tools. *J. Phys. Condens. Matter* **32**, 015901 (2020).
98. Fisher, D. S. & Lee, P. A. Relation between conductivity and transmission matrix. *Phys. Rev. B* **23**, 6851–6854 (1981).
99. Büttiker, M., Imry, Y., Landauer, R. & Pinhas, S. Generalized many-channel conductance formula with application to small rings. *Phys. Rev. B* **31**, 6207–6215 (1985).

Acknowledgements

This work was supported by the National Natural Science Foundation of China (Grant Nos. 12374172, 11974045, 61888102), the National Key Research and Development Program of China (Grants No. 2020YFA0308800), “Strategic Priority Research Program (B)” of the Chinese Academy of Sciences (Grant No. XDB30000000). The computational resources were provided by the Shanghai Supercomputing Center.

Author contributions

J.-T.S. and H.-J.G. directed the project. M.L. performed the DFT calculations, analyzed the results, and developed the conclusions. M.L. and J.-T.S. wrote the manuscript. S.H. and Z.J. helped calculate the spin-polarized transport of two-probe devices. H.J. and J.G. participated in the discussion and cowrite the paper.

Competing interests

The authors declare no competing interests.

Additional information

Supplementary information The online version contains supplementary material available at <https://doi.org/10.1038/s41524-024-01369-5>.

Correspondence and requests for materials should be addressed to Jia-Tao Sun.

Reprints and permissions information is available at <http://www.nature.com/reprints>

Publisher's note Springer Nature remains neutral with regard to jurisdictional claims in published maps and institutional affiliations.

Open Access This article is licensed under a Creative Commons Attribution-NonCommercial-NoDerivatives 4.0 International License, which permits any non-commercial use, sharing, distribution and reproduction in any medium or format, as long as you give appropriate credit to the original author(s) and the source, provide a link to the Creative Commons licence, and indicate if you modified the licensed material. You do not have permission under this licence to share adapted material derived from this article or parts of it. The images or other third party material in this article are included in the article's Creative Commons licence, unless indicated otherwise in a credit line to the material. If material is not included in the article's Creative Commons licence and your intended use is not permitted by statutory regulation or exceeds the permitted use, you will need to obtain permission directly from the copyright holder. To view a copy of this licence, visit <http://creativecommons.org/licenses/by-nc-nd/4.0/>.

© The Author(s) 2024